

## Article

# Dynamic Climate Influence on Magnesium Isotope Variation in Saline Lacustrine Dolomite: A Case Study of the Qianjiang Formation, Jiangnan Basin

Tianyu Wang<sup>1</sup>, Kun Ling<sup>1</sup>, Ren Wei<sup>1,2</sup>  and Lin Dong<sup>1,\*</sup>

<sup>1</sup> School of Earth and Space Sciences, Peking University, Beijing 100871, China; 2101110663@pku.edu.cn (T.W.); sqlingkun@pku.edu.cn (K.L.); wr1996@pku.edu.cn (R.W.)

<sup>2</sup> Institute of Energy, Peking University, Beijing 100871, China

\* Correspondence: lin.dong@pku.edu.cn

**Abstract:** The investigation of magnesium (Mg) isotopes in dolomite has mainly focused on marine dolomite environments, leaving a significant gap in the understanding of their dynamics within lacustrine settings, especially in saline lake basins. In this study, a total of 16 sediment core samples from Well BX-7 in the Qianjiang Depression were sequentially selected for scanning electron microscope observation, whole-rock analysis for major and minor elements, and isotopic measurements including  $\delta^{18}\text{O}_{\text{carb}}$ ,  $\delta^{13}\text{C}_{\text{carb}}$ ,  $\delta^{26}\text{Mg}_{\text{dol}}$ , and  $\delta^{26}\text{Mg}_{\text{si}}$ . In addition, two intact cores were subjected to detailed analysis on the centimeter scale. Sedimentation models were established to elucidate dolomite formation under contrasting climatic conditions, specifically humid climates with a significant riverine Mg input versus relatively dry conditions with a lower Mg input. Furthermore, a quantitative model was developed to assess the magnesium flux and isotopic mass balance within lacustrine systems, simulating the magnesium isotope variations in lake water under different climatic scenarios. The dolomite sample data at a smaller scale (sampling interval  $\approx 3\text{--}5$  mm) demonstrate a consistent trend with the established model, providing additional confirmation of its reliability. Dolomite precipitated under humid climatic conditions exhibits a lower and relatively stable  $\delta^{26}\text{Mg}_{\text{dol}}$ , lower  $\delta^{18}\text{O}$ , and higher CIA, indicating higher river inputs and relatively stable Mg isotope values of lake water controlled by river input. Nevertheless, dolomite formed under relatively dry climatic conditions shows a relatively high  $\delta^{26}\text{Mg}_{\text{dol}}$ , higher  $\delta^{18}\text{O}$ , and lower CIA, suggesting reduced river inputs and weathering intensity, as well as relatively high magnesium isotope values of the lake water controlled by dolomite precipitation. This study contributes to the understanding of magnesium isotopes in lacustrine dolomite systems.

**Keywords:** Mg isotopes; lacustrine dolomite; saline lake; paleoclimate



**Citation:** Wang, T.; Ling, K.; Wei, R.; Dong, L. Dynamic Climate Influence on Magnesium Isotope Variation in Saline Lacustrine Dolomite: A Case Study of the Qianjiang Formation, Jiangnan Basin. *Minerals* **2024**, *14*, 459. <https://doi.org/10.3390/min14050459>

Academic Editors: Yong Sik Gihm, Taejin Choi and Byung Choon Lee

Received: 16 March 2024

Revised: 19 April 2024

Accepted: 25 April 2024

Published: 26 April 2024



**Copyright:** © 2024 by the authors. Licensee MDPI, Basel, Switzerland. This article is an open access article distributed under the terms and conditions of the Creative Commons Attribution (CC BY) license (<https://creativecommons.org/licenses/by/4.0/>).

## 1. Introduction

Dolomite (i.e., calcium magnesium carbonate,  $\text{CaMg}(\text{CO}_3)_2$ ) stands as a pivotal sedimentary rock in pre-Palaeozoic and Palaeozoic epochs [1]. Since Déodat de Dolomieu's 1791 discovery of dolomite [2], the enigma surrounding dolomite has persistently baffled geologists for over two centuries [3]. Dolostones, constituting a crucial subset of carbonate rock reservoirs for oil and gas, play a crucial role in hydrocarbon exploration [4,5]. Nevertheless, the formation mechanisms of dolomite remain unclear, leading to significant uncertainties in characterizing and predicting dolomite reservoirs [4]. Over the past two decades, advancements in multi-collector inductively coupled plasma mass spectrometry (MC-ICP-MS) have enabled exceptionally precise isotope analysis for various metals, including Mg [6–8]. At present, the research on dolomite Mg isotopes primarily focuses on the following two aspects: (1) Tracing the origin of  $\text{Mg}^{2+}$  in dolomite. Mg isotopes exhibit significant fractionation during low-temperature geochemical processes, leading to pronounced differences in the Mg isotope composition among various surface reservoirs,

such as igneous rocks, carbonate rocks, clay minerals, seawater, river water, porewater, and hydrothermal fluids [9–14]. (2) Based on the variations in dolomite magnesium isotopes, quantitative or semi-quantitative studies are conducted to determine potential sources of dolomitizing fluids and to establish corresponding dolomitization models. Currently, DAR and Raley fractionation models have been developed within marine dolomite to quantitatively constrain dolomite origins [15,16]. These models, in conjunction with sequence stratigraphy, have effectively elucidated the genesis of thick dolomite layers [17].

Lacustrine dolomite, compared to marine dolomite, exhibits a lesser distribution in the geological record, thus having fewer prior related studies. As mentioned above, previous studies on magnesium isotopes in dolomite have primarily focused on marine dolomite, with lacustrine environments, especially in saline lake basins, receiving relatively limited scrutiny. Recently, there has been a gradual increase in geochemical research focusing on the carbonate constituents in lacustrine carbonate [18–21]. For instance, carbon and oxygen isotopes in carbonates have been employed to reconstruct ancient environments [22], while Mg isotopes of halite serve as a sensitive indicator for drying and recharging events in terrestrial saline lakes [23]. In addition, there has been corresponding progress on the origin of dolomite in lagoons with higher salinity [24,25].

Substantial disparities exist in the depositional environments and formation mechanisms of lacustrine and marine dolostones. Most of these lacustrine dolomites are interpreted as primary or quasi-syngenetic deposits, even though the physical and chemical conditions (salinity, pH, alkalinity, Mg/Ca) for the formation of lacustrine dolomites vary [26–39]. River waters exhibit notable variations in Mg isotopes, impacting the dolomitization process differently in lacustrine and marine settings [40,41]. Saline lake basins, characterized by much smaller volumes and correspondingly significantly reduced magnesium reservoirs compared to oceans, further emphasize the impact of river inputs and dolomite sedimentation on Mg isotopes of lake water. In contrast, marine environments, with their larger size and more extensive magnesium reservoirs, possess greater resilience against such impacts. Additionally, the rock compositions in lake basins are notably more intricate, typically including three major components: clastic, carbonate, and evaporites [18,42,43]. Furthermore, diagenesis occurs more frequently in lake deposits, often at the centimeter and millimeter scales. Therefore, it is imperative to conduct further investigation into the geochemical systems of lacustrine dolomite across different scales.

The Qianjiang Formation of the Jiangnan Basin mainly consists of mixed deposits, including clastic, carbonate, and evaporite constituents, collectively defined as “mixed sedimentary rocks”. In order to understand the formation mechanism and the controlling factors of the lacustrine dolomite, in this study, we conducted major and trace element and isotope analyses of the carbonate and clastic components, at both the meter and centimeter scales.

## 2. Geological Settings

The Jiangnan Basin, situated within Hubei Province, China, spans approximately 2530 square kilometers and represents a rift basin formed on the Palaeozoic and Mesozoic basement during the Cretaceous to Neogene periods [44–46]. The Qianjiang Depression, located in the central part of the Jiangnan Basin, is a faulted depression delineated by various geological structures. It is bounded to the northwest by the Yonglonghe Uplift, the Hanshui Depression, the Lexiangguan horst, and the Jingmen Depression. To the southeast, it is bordered by the Tonghaikou Uplift, while to the northeast, it is adjacent to the Yuekou Low Uplift. It is delineated by the Yajiao-Xingou Low Uplift to the southwest (Figure 1) [47,48].

The basement of the Qianjiang Depression comprises Precambrian metamorphic rocks, Silurian to Early Triassic marine sedimentary strata, and Middle Triassic to Jurassic fluvial deposits [47]. The overlying lacustrine strata are the Paleogene Jinghezhen Formation and the Neogene Guanghuasi and Pingyuan formations [49]. The Qianjiang Depression exhibits the highest subsidence rate in the Jiangnan Basin. During the deposition of the

Qianjiang Formation, the basin underwent intense evaporation, fostering a high salinity level and a closed environmental setting. The salts manifest alternating layers with mixed sedimentary rocks and salt rocks, displaying clear vertical rhythm and consistent lateral continuity. Vertically, the Qianjiang Formation can be further divided into four stratigraphic units, i.e., Eq<sup>4</sup> to Eq<sup>1</sup> from the bottom to top. The Qianjiang 2–4 Members primarily comprise alternating layers of halite-glauberite, carbonate, and shale in the depocenter of the Qianjiang Depression [50]. Typically, carbonate sedimentation occurs in situ within lacustrine or shallow marine environments, whereas siliciclastic sediment is primarily transported into the system by rivers [51]. Recent studies indicate that the mixed sediments in Qian 3<sup>4</sup> section (this study) can be divided into two types: siliciclastic-dominated mixed sediment and carbonate-dominated mixed sediment. These variations are indicative of consistent fluctuations in the overall balance between water inflow/outflow [22]. Therefore, the degree of fluvial input and weathering processes affecting mixed sediments in the Qianjiang region varies across different lithologies.

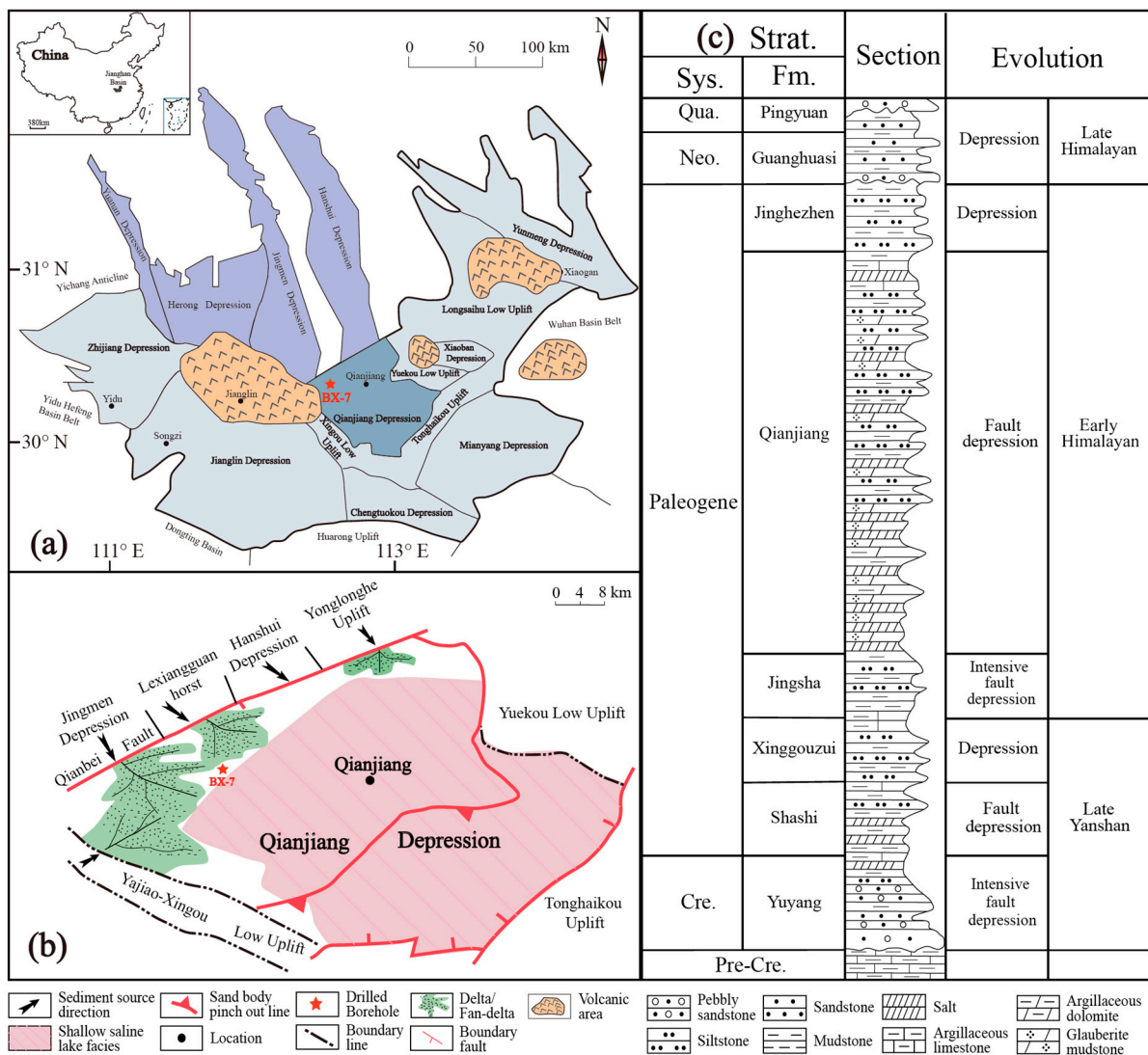


**Figure 1.** Geological setting and stratigraphic column of the Qianjiang Depression, Jiangnan Basin. (a) The location of the Qianjiang Depression, Jiangnan Basin (modified from Fang et al., 2014; Huang et al., 2014 [47,48]); (b) sedimentary lithofacies of the Eocene Qianjiang Formation in the Qianjiang Depression (modified from Huang et al., 2014; Wei et al., 2023 [22,47]); (c) the stratigraphic column of the Qianjiang Depression (modified after Shen et al., 2019 [52]).

### 3. Materials and Methods

In this study, a total of 16 sediment core samples from Well BX-7 in the Qianjiang Depression were selected for elemental composition and stable isotope measurements (L1) (Figure 2). Two of the 16 sediment cores (C1 and C2) were selected for refined geochemical sampling and analysis with samples collected at intervals of 3–5 mm. All the powder samples including L1, C1, and C2 were prepared using hand-held microdrills for measuring major elements and trace elements and carbon, oxygen, and Mg isotopes. In addition, we conducted major and trace element analysis on the supernatant obtained after the first deionized water wash centrifugation of samples C1 and L1–13.

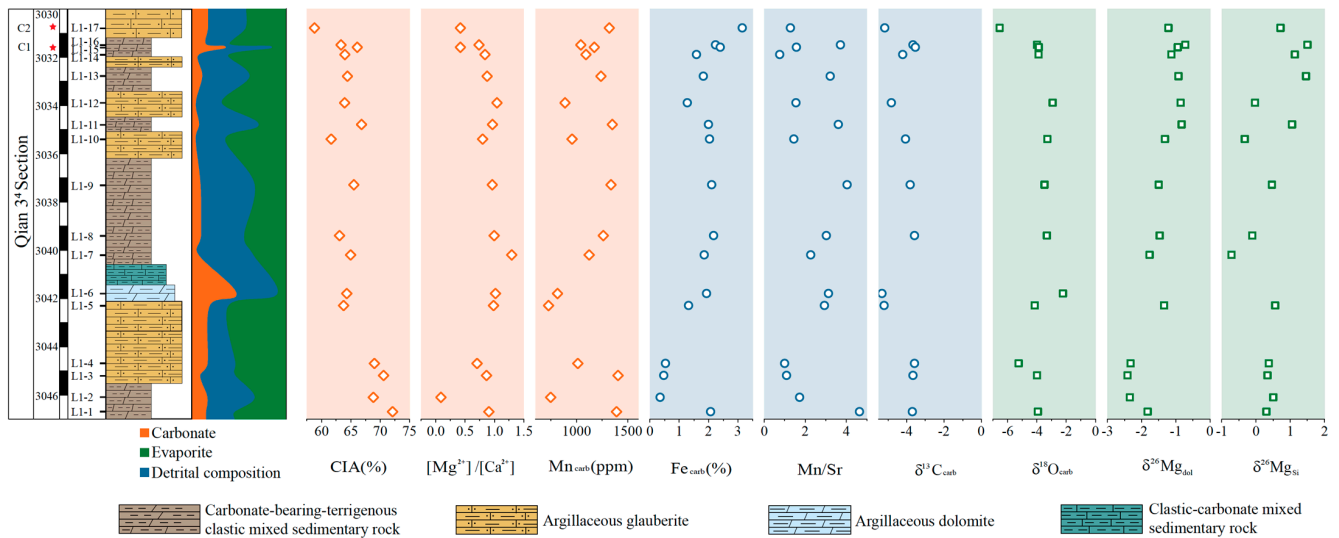


**Figure 2.** Chemostratigraphic profiles of CIA,  $[Mg^{2+}]/[Ca^{2+}]$ , [Mn], [Fe], [Mn]/[Sr],  $\delta^{13}C_{carb}$ ,  $\delta^{18}O_{carb}$ ,  $\delta^{26}Mg_{dol}$ , and  $\delta^{26}Mg_{Si}$  values of Well BX-7 from the Qianjiang Depression, Jiangnan Basin. The sampling locations of two cores for centimeter-scale geochemical analysis are marked with red pentagrams.

#### 3.1. Elemental Composition Analyses

Approximately 100 mg of powder from each sample was placed into a 10 mL centrifuge tube and washed three times each with deionized water and 10% NaCl. After the first deionized water wash, 0.5 mL of supernatant from samples C1 and L1-5 was mixed with 4.5 mL of 2% HNO<sub>3</sub> in preparation for major and trace element analysis of evaporites. The testing method for evaporite in this study was solely to roughly confirm the magnesium content in evaporite, without converting it into ppm (mass ratio).

Then, 10 mL 0.5 N acetic acid was added into each centrifuge tube and was placed in an ultrasonic bath for 30 min at 50 °C for three times. The dissolution method ensures complete dissolution of carbonate minerals without affecting oxides and sulfides. Following centrifugation, 0.5 mL supernatant was collected and then added into 4.5 mL 2% HNO<sub>3</sub> for elemental composition analysis of carbonate fraction. The remaining supernatant was preserved for pre-treatment prior to magnesium isotope analysis of dolomite.

Residue was washed by 5 mL 1 N hydrochloric acid quickly. After centrifugation, the residue was washed with Milli-Q water five times, and then dried down at 70 °C in an oven. Then, the dried residue was dissolved in a mixture of 3 mL concentrated HF and 1 mL concentrated HNO<sub>3</sub> in a 5 mL Teflon beaker. Afterward, the airtight baker was heated for 24 h at 120 °C, then the solution was evaporated on a hotplate to expel unreacted acid. Then, the residual was dissolved in 5 mL concentrated HNO<sub>3</sub> for 24 h at 120 °C. If the solution cleared up, then the solution was evaporated. Otherwise, repeat the dissolution procedure as described above. After evaporation, 5 mL 2% HNO<sub>3</sub> was added into the beaker and the solution was transferred into a test tube for analysis then 0.5 mL supernatant was collected and added into 4.5 mL 2% HNO<sub>3</sub> for elemental composition

analysis of siliciclastic component. Finally, the remaining supernatant was preserved for pre-treatment before magnesium isotope testing of clastic components.

Major and minor element contents of samples from C1 were measured by Spectra Blue Sop Inductively Coupled Plasma Optical Emission Spectrometry (ICP-OES) at Peking University. The detailed analytical procedure of ICP-OES analyses has been reported in a previous publication [15], and the analytical precision of major and minor elements (e.g., Ca, Mg, Fe, Mn, Al, K, Na, etc.) is better than 5%. The major and minor element contents of samples from L1 and C2 were measured by Jena PQ MS at Beijing Kehui Testing Technology Co., Ltd., Beijing, China. The analytical precision of major and minor elements (e.g., Ca, Mg, Fe, Mn, Al, K, Na, etc.) is also better than 5%.

### 3.2. Carbon and Oxygen Isotopes

About 0.2 mg of 200 mesh carbonate powder was taken and placed in a 10 mL headspace bottle, helium was passed in (He, purity 99.999%) to drive out the air in the bottle, and 1 mL anhydrous phosphoric acid ( $\text{H}_3\text{PO}_4$ , purity 100%) was injected and reacted for 2 h in the Gas Bench II at 70 °C. The generated carbon dioxide was extracted by the automatic sampler (GC PAL autosampler and sample tray) and underwent gas chromatography (GC: gas chromatography, 70 °C) for separation and then was passed into the isotope ratio mass spectrometer (Thermo Scientific Delta V Plus), which was used to obtain its oxygen isotope and carbon isotope composition relative to the standard gas. Isotope ratios are reported in the  $\delta$  notation with respect to Vienna Pee Dee Belemnite (V-PDB), and were calibrated on internal standard calcium carbonate (Warcalcium carbonate):  $\delta^{13}\text{C} = 0.13\text{‰}$ ,  $\delta^{18}\text{O} = -8.18\text{‰}$ , which is calibrated on NBS19 ( $\delta^{13}\text{C} = 1.95\text{‰}$ ,  $\delta^{18}\text{O} = -2.20\text{‰}$ ). Analytical precisions are 0.1‰ for  $\delta^{13}\text{C}$  and 0.2‰ for  $\delta^{18}\text{O}$ , respectively.

### 3.3. Purification and Testing of Mg Isotopes

The purification and testing of Mg isotopes were carried out at the ultra-clean laboratory of Beijing Kehui Testing Technology Co. Ltd. The supernatant of the carbonate and siliceous fractions from the previous step was retrieved with the objective of achieving a magnesium content of 20  $\mu\text{g}$ . After evaporation, weighted powders were dissolved in 15 mL Savillex Teflon beakers with a mixture of ultra-pure concentrated HF-HNO<sub>3</sub> (3:2, v/v).

The capped beakers were placed on a 150 °C hot plate for 2 to 3 days. After the initial digestion and evaporation to dryness, the samples were treated with 2 mL of HNO<sub>3</sub> and 3 mL of HCl. The solutions were evaporated to dryness the following day. Subsequently, the samples were refluxed with 3 mL of concentrated HNO<sub>3</sub> to remove residual fluorides and finally dissolved in 1 mL of 2 N HNO<sub>3</sub> for chromatographic column chemistry.

Mg purification was performed in Savillex microcolumns (6.4 mm ID  $\times$  9.6 mm OD, 30 mL reservoir) loaded with 2 mL of Bio-Rad AG50W-X12 (200~400 mesh) cation resin. Details of the Mg separation procedure are shown in Table 1. We repeated the procedure twice when K/Mg > 2:1. After the chemical purification, Mg elution was evaporated to dryness. The residues were dissolved in 2% (m/m) HNO<sub>3</sub> for isotope ratio measurement. The total procedural Mg blank, including sample digestion and chromatographic procedures, was lower than 10 ng, which is negligible relative to the amount of Mg (20  $\mu\text{g}$ ) processed through the column procedure.

Before the measurement, 1 ppm IGGMG1 (internal standard sample in the laboratory) was used to optimize the instrument parameters to ensure that the signal strength of <sup>24</sup>Mg was approximately 10 V ppm<sup>-1</sup>. Finally, the Mg isotopic ratios were normalized to the international DSM3 Mg [53]. In order to assess the quality of the mass spectrometric analyses, in-house standard GSB Mg [54] was analyzed every five samples. The  $\delta^{26}\text{Mg}$  mean value of the GSB Mg standard solutions was  $-2.026 \pm 0.056$  (2SD, n = 24) in this analytical session. The carbonate fraction and siliciclastic component of GSR-6, GSR-12, and GSR-30 were  $-1.761 \pm 0.008$  and  $-1.896 \pm 0.018$ ;  $-2.082 \pm 0.002$  and  $-0.915 \pm 0.030$ ; and  $-2.022 \pm 0.050$  and  $-1.042 \pm 0.047$ , respectively.

**Table 1.** Details of Mg separation procedure.

Elute	Volume (mL)	Comments
Milli Q H <sub>2</sub> O	15~20	Backwash to remove air bubbles and reduce resin compaction
4 N HNO <sub>3</sub> + 0.5 N HF	4	Cleaning resin alternatively for three times
Milli-Q H <sub>2</sub> O	4	
2 N HNO <sub>3</sub>	2 × 2	Resin conditioning
Sample in 2 N HNO <sub>3</sub>	1	Sample loading
2 N HNO <sub>3</sub> + 0.5 HF	5	Removing matrix
1 N HNO <sub>3</sub>	8	
1 N HNO <sub>3</sub>	1	Before cut collection
1 N HNO <sub>3</sub>	24	Mg Collection
1 N HNO <sub>3</sub>	1	Post cut collection
Milli Q H <sub>2</sub> O	5	Recovering resin

## 4. Results

### 4.1. Petrological Characteristics

The microscopic observation of the thin sections and the analysis of the scanning electron microscopy reveal the primary minerals include carbonate minerals (calcite, dolomite, etc.), detrital minerals (quartz, feldspar, clay minerals, etc.), and evaporites (glauberite, etc.) (Figure 3). Based on the mineral compositions and their relative abundance, four lithological types were identified, including argillaceous glauberite, argillaceous dolomite, carbonate-bearing terrigenous clastic mixed rock and clastic-carbonate mixed rock.

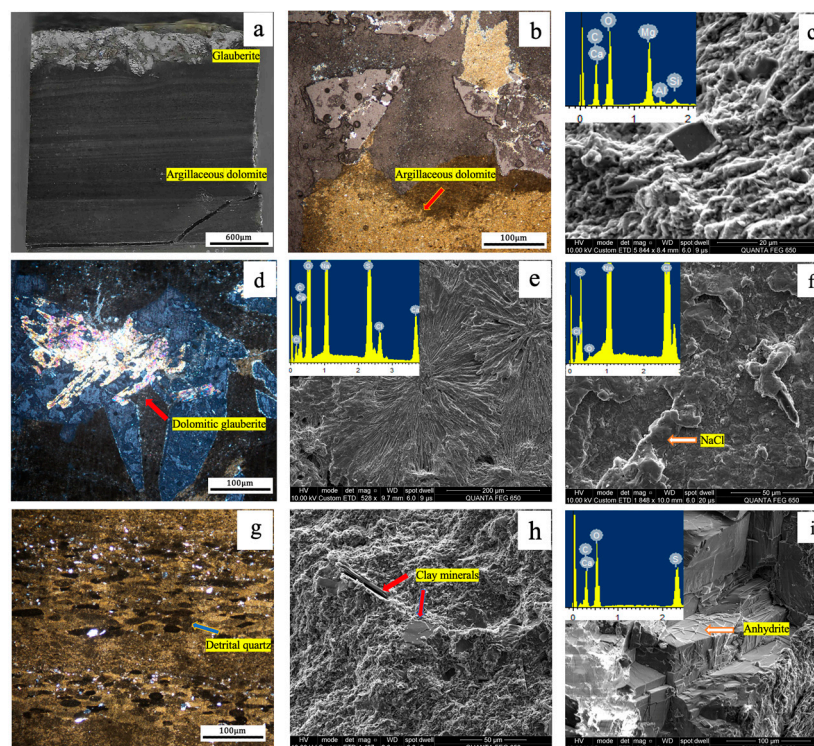


**Figure 3.** (a) Photograph of argillaceous dolomite and glauberite from C1; (b) micrograph of argillaceous dolomite and glauberite; (c) SEM image of dolomite crystals from C2; (d) glauberite crystals were cemented by dolomite; (e) SEM image of radiating glauberite; (f) NaCl crystals covering the surface of thin section of rock; (g) detrital quartz grains in argillaceous dolomite; (h) SEM image of clay minerals; (i) SEM image of anhydrite crystals.

The micritic dolomite appears predominantly gray to dark gray, with some instances of gray-black, often exhibiting thin layering (Figure 3a). It is interspersed with millimeter-scale bands, typically composed of detrital quartz (Figure 3g). The micritic dolomite and clastic materials are intermixed to form the matrix, with larger mirabilite crystals scattered throughout (Figure 3b). The microscopic observations reveal dolomite with a micritic structure, displaying poorly defined crystal forms and frequently containing variable amounts of terrestrial particles (Figure 3g).

#### 4.2. Geochemical Characteristics

##### 4.2.1. Elemental Geochemistry

The chemical compositions of the water-soluble components of the evaporite samples in C1 and L1-5 are shown in Table S1. The evaporites have high concentrations of Na and Ca, with a low Mg content, mainly composed of glauberite. The major and trace elemental compositions of the carbonate and silicate components of L1, C1, C2 are shown in Table S2. The main elements and isotopic characteristics of L1 can be found in Table 2. The  $[\text{Fe}_{\text{carb}}]$  and  $[\text{Mn}_{\text{carb}}]$  of the samples L1, C1, and C2 range from 0.35% to 3.4%, with an average of 2.11% ( $n = 51$ ), and 727.74 ppm ~1405.00 ppm, with an average of 1099.87 ppm ( $n = 51$ ). The  $[\text{Al}_{\text{Si}}]$ ,  $[\text{Mg}_{\text{Si}}]$ ,  $[\text{Mg}_{\text{Si}}]/[\text{Al}_{\text{Si}}]$  (molar), and CIA of the samples L1, C1, C2 range from 4.43% to 9.85% (average 8.56%,  $n = 51$ ); 0.45% to 5.32% (average 1.66%,  $n = 51$ ); 0.08 to 0.80 (average 0.22,  $n = 51$ ); and 57.22% to 72.10% (average 62.74%,  $n = 51$ ). The relatively low CIA values observed in only two samples within C2, specifically, 48.05% and 36.09%, could be attributed to the low silicate component, with a small amount of calcium magnesite being incorporated. While the major and trace elemental compositions of the carbonate and silicate components of L1, C2, and C1 were performed in a different laboratory, the consistency of  $[\text{Fe}_{\text{carb}}]$ ,  $[\text{Mn}_{\text{carb}}]$ ,  $[\text{Al}_{\text{Si}}]$ , and  $[\text{Mg}_{\text{Si}}]$  attest to the accuracy of the analytical method.

**Table 2.** Major and trace element and isotope data of L1 (complete data are provided in Supplementary Table S2).

Sample No.	Depth m	Carb %	CIA %	$[\text{Mg}^{2+}]/[\text{Ca}^{2+}]$	$\text{Mn}_{\text{carb}}$ (ppm)	$\text{Fe}_{\text{carb}}$ (%)	Mn/Sr	$\delta^{13}\text{C}_{\text{carb}}$	$\delta^{18}\text{O}_{\text{carb}}$	$\delta^{26}\text{Mg}_{\text{dol}}$	$2\sigma$	$\delta^{26}\text{Mg}_{\text{Si}}$	$2\sigma$
L1-17	3030.80	15.97	58.80	0.42	1318.00	3.15	1.28	-5.17	-6.53	-1.21	0.003	0.72	0.720
L1-16	3031.50	14.27	63.33	0.74	1042.12	2.24	3.72	-3.66	-3.98	-0.72	0.044	1.50	1.504
L1-15	3031.60	34.95	66.09	0.42	1172.00	2.40	1.57	-3.53	-3.87	-0.94	0.017	-	-
L1-14	3031.90	5.91	64.00	0.84	1091.97	1.59	0.76	-4.21	-3.87	-1.13	0.006	1.14	1.138
L1-13	3032.80	9.83	64.41	0.88	1237.28	1.82	3.22	-	-	-0.92	0.018	1.46	1.460
L1-12	3033.90	3.00	63.95	1.05	888.20	1.28	1.56	-4.81	-2.91	-0.86	0.053	-0.03	-0.026
L1-11	3034.80	6.46	66.84	0.97	1348.56	2.00	3.62	-	-	-0.83	0.033	1.05	1.055
L1-10	3035.40	2.77	61.65	0.80	957.10	2.03	1.45	-4.06	-3.28	-1.31	0.011	-0.33	-0.326
L1-9	3037.30	7.93	65.53	0.97	1335.40	2.10	4.04	-3.81	-3.47	-1.50	0.053	0.47	0.466
L1-8	3039.40	8.45	63.08	1.00	1260.20	2.18	3.03	-3.58	-3.32	-1.47	0.045	-0.10	-0.104
L1-7	3040.20	5.69	64.97	1.30	1122.79	1.85	2.27	-	-	-1.76	0.057	-0.71	-0.712
L1-6	3042.00	46.51	64.30	1.02	815.19	1.93	3.14	-5.32	-2.21	-	-	-	-
L1-5	3042.30	17.77	63.78	0.98	727.74	1.32	2.94	-5.21	-4.15	-1.34	0.019	0.56	0.559
L1-4	3044.70	15.52	69.01	0.71	1013.19	0.53	1.00	-3.57	-5.24	-2.32	0.055	0.37	0.373
L1-3	3045.20	7.51	70.60	0.86	1405.07	0.47	1.09	-3.66	-3.98	-2.40	0.052	0.34	0.337
L1-2	3046.10	15.45	68.82	0.09	747.24	0.35	1.73	-	-	-2.34	0.020	0.50	0.505
L1-1	3046.70	13.94	72.10	0.91	1390.01	2.07	4.64	-3.69	-3.92	-1.82	0.042	0.31	0.306
GSR-6										-1.76	0.008	-0.915	0.030
GSR-12										-2.08	0.002	-1.042	0.047
GSR-30										-1.90	0.018	-2.022	0.050

##### 4.2.2. Stable Isotopes

The  $\delta^{13}\text{C}_{\text{carb}}$  and  $\delta^{18}\text{O}_{\text{carb}}$  values of L1, C1, and C2 are plotted in Figure 4. The  $\delta^{13}\text{C}_{\text{carb}}$  and  $\delta^{18}\text{O}_{\text{carb}}$  values range from  $-5.91\text{‰}$  to  $-3.02\text{‰}$  (average  $-3.99\text{‰}$ ,  $n = 50$ ) and  $-6.53\text{‰}$  to  $-2.85\text{‰}$  (average  $-4.65\text{‰}$ ,  $n = 50$ ), respectively. The  $\delta^{26}\text{Mg}_{\text{dol}}$  and  $\delta^{26}\text{Mg}_{\text{Si}}$  of L1 range from  $-2.41\text{‰}$  to  $-0.72\text{‰}$  (average  $-1.46\text{‰}$ ,  $n = 15$ ) and  $-0.71\text{‰}$  to  $1.50\text{‰}$  (average  $0.48\text{‰}$ ,

n = 15). The  $\delta^{26}\text{Mg}_{\text{dol}}$  of C1 and C2 ranges from  $-0.97\text{‰}$  to  $-0.70\text{‰}$  (average  $-0.79\text{‰}$ , n = 17) and  $-1.23\text{‰}$  to  $-1.13\text{‰}$  (average  $-1.20\text{‰}$ , n = 4), respectively.

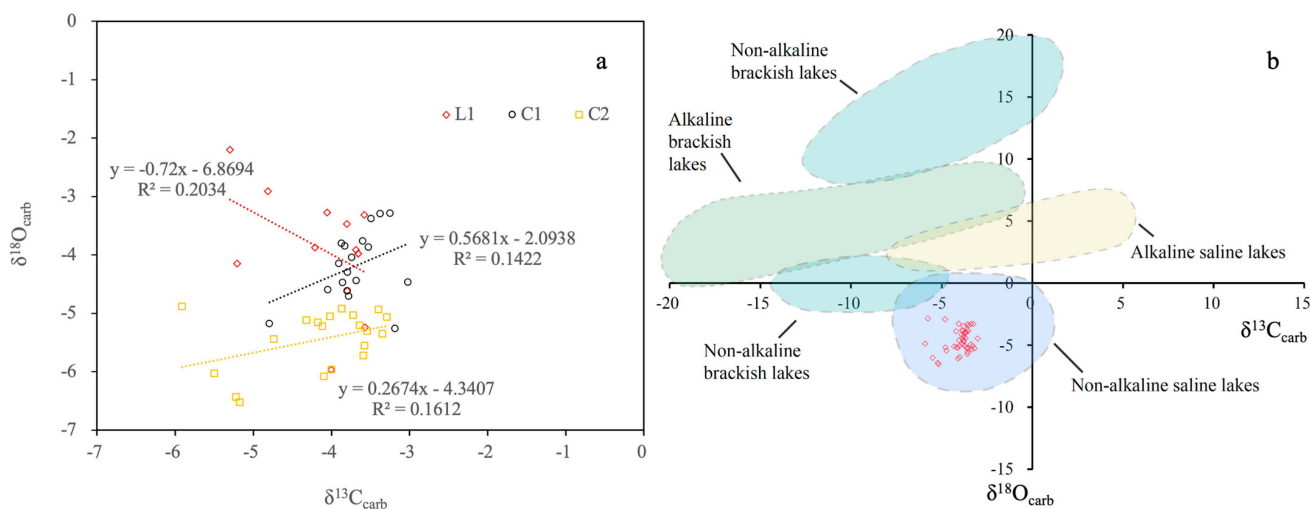


**Figure 4.** (a) Results of the stable oxygen and carbon isotope analysis of L1, C1, and C2; (b) Results of the stable oxygen and carbon isotope values of L1, C1, and C2 suggest that the Jiangnan Basin is a non-alkaline saline lake (modified from Guo et al., 2023 [21]).

## 5. Discussion

### 5.1. Paleoclimate and Basin Provenance

#### 5.1.1. Assessing the Impact of Diagenesis

The correlation coefficient between the  $\delta^{18}\text{O}_{\text{carb}}$  and  $\delta^{13}\text{C}_{\text{carb}}$  values is a crucial indicator for assessing the degree of diagenetic alteration. A strong positive correlation is frequently interpreted as evidence of substantial mixing between meteoric groundwater and pore fluids in paleolake sediments [55,56]. In addition, the elemental concentrations of  $\text{Sr}^{2+}$  and  $\text{Mn}^{2+}$  are also employed to assess the diagenetic alteration [57]. During diagenesis,  $\text{Mn}^{2+}$  is incorporated into carbonate minerals, while  $\text{Sr}^{2+}$  is expelled, leading to an elevated Mn/Sr ratio. Carbonates with Mn/Sr < 10 are typically considered to preserve the original geochemical signature of the water column [58].

In our samples, no obvious linear correlation is observed between  $\delta^{18}\text{O}_{\text{carb}}$  and  $\delta^{13}\text{C}_{\text{carb}}$  (Figure 4). The Mn/Sr ratios of the samples in L1, C1, and C2 range from 0.76 to 4.64 (average 2.42), 0.6 to 3.0 (average 1.84), and 0.06 to 5.88 (average 2.52), respectively. These results suggest that the selected samples have undergone minimal diagenetic alterations, and their geochemical signatures closely reflect the original conditions of the lake water.

#### 5.1.2. Paleoclimate Characteristics

The continental weathering process occurring in the provenance serves as a precursor to the subsequent sedimentary processes, significantly influencing the geochemical composition of terrestrial sediments [59]. Thus, the terrestrial clastic components within the sediments can reflect the paleoclimate, weathering trend, and recycling effects of source rocks [60]. The chemical index of alteration (CIA), which quantitatively evaluates the weathering conditions of the provenance, is an effective indicator for evaluating the intensity of continental weathering [61]. The CIA is calculated as follows:  $\text{CIA} = \text{molar}[(\text{Al}_2\text{O}_3)/(\text{Al}_2\text{O}_3 + \text{CaO}^* + \text{Na}_2\text{O} + \text{K}_2\text{O})] \times 100$ , where  $\text{CaO}^*$  indicates the amount of CaO in silicate minerals [62]. In this study, the CIA values within the 3044–3046 m sediment section are relatively higher compared to those in the sediment section from 3031 to 3043 m (Figure 2), indicating a relatively stronger weathering intensity.

Carbonate oxygen isotopes can reflect hydrological changes in lakes induced by precipitation and evaporation. An increase in the  $\delta^{18}\text{O}$  values is indicative of increased evaporation and reduced precipitation, and vice versa [63]. The temperature may also affect

$\delta^{18}\text{O}$ , but compared to the changes caused by evaporation and precipitation, the impact of these changes is relatively minor [22]. The  $\delta^{18}\text{O}$  values of the 3044–3046 m sediment section are relatively lower than the 3031–3043 m sediment section (Figure 2), which indicates a humid climate with more precipitation.

### 5.1.3. Basin Provenance

Siliciclastic deposits found in saline lakes usually originate from weathered bedrock surrounding the basin, transported by river or wind. Consequently, the geochemical features of the siliciclastic deposits can be influenced by the diverse compositions of the source rocks. Previous studies have reported the widespread distribution of granites in the Qinling–Dabie orogenic belt to the north and the Jiangnan orogenic belt to the south of the Jiangnan Basin [64]. Additionally, sediments in the sixth and eighteenth rhythmic layers of the Qian 4 section are primarily derived from felsic volcanic rocks, with the eighteenth rhythmic layer also containing compositions from basalt and andesite sources [45].

Trace elements, such as La, Th, Hf, Co, and Sc, are widely regarded as reliable indicators of the provenance of clastic sediments due to their low mobility during post-depositional alterations [65,66]. Both trace elemental ratios, such as La/Sc, La/Th, Th/Sc, Zr/Sc, and Th/Co, known for their sensitivity in provenance determination, along with  $\delta\text{Eu}$ , exhibit negligible variations. The REE characteristics of siliciclastic deposits display no evident disparities either. These findings suggest a relatively consistent provenance for the following deposition process [67].

As depicted in Figure 5, the plot of La/Th against Hf emerges as an effective means of discriminating between diverse sources in bulk rocks. Sediments sourced from acid-dominated arcs consistently exhibit low La/Th ratios and Hf contents within the 3–7 ppm range [68]. In Figure 5, the majority of our samples are plotted in or close to the felsic source fields, indicating that the source materials were dominated by felsic rocks with a presence of mafic components.

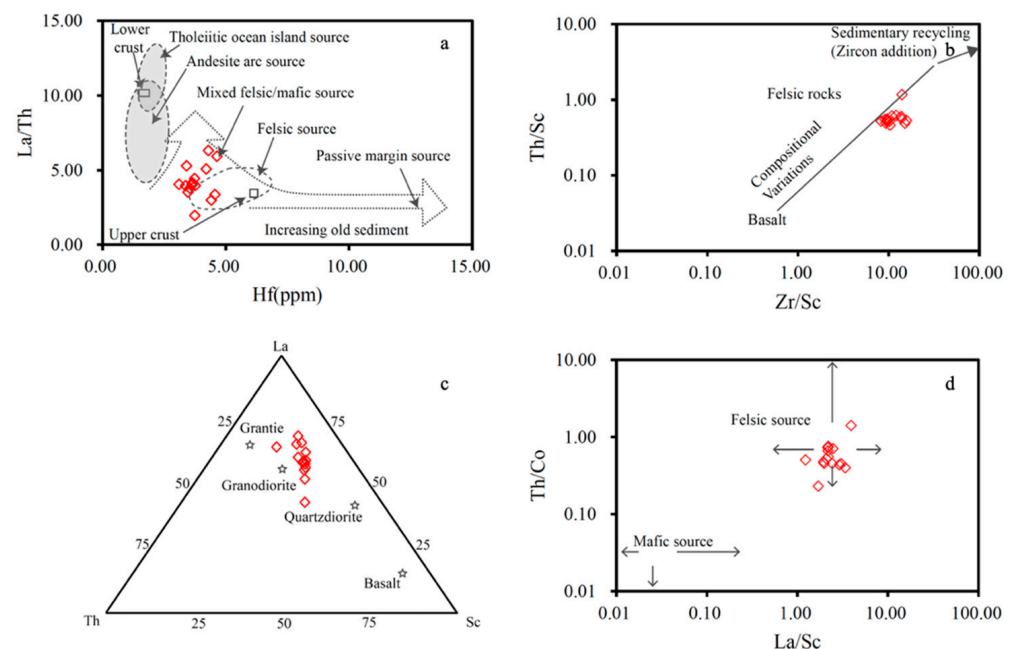


**Figure 5.** Provenance analyses of the Qian 3<sup>4</sup> (The samples are from L1.) in the Qianjiang Depression. (a) La/Th versus Hf (modified after P et al., 1987 [68]); (b) Th/Sc versus Zr/Sc (modified after Kong et al., 1993 [45]); (c) La-Th-Sc ternary diagram (modified after Cullers et al., 2000 [67]); (d) Th/Co versus La/Sc (modified after Cullers et al., 2002 [69]).

## 5.2. Dolomite Deposition Pattern in Saline Lake

### 5.2.1. $\delta^{26}\text{Mg}$ of the River

In the investigation of marine dolostone, magnesium isotopes are predominantly influenced by dolomitization fluids, fractionation coefficients, and dolomitization patterns [15,16,70]. In lacustrine dolostone, however, we introduce another significant factor—river inputs. This is mainly due to the lower proportion of carbonates in lacustrine mixed sediments and the comparatively smaller magnesium reservoir in lakes, underscoring the influence of river inputs in regulating dolomite in lacustrine mixed sediments under humid climates.

Silicate weathering is predominantly marked by the dissolution and alteration of pristine silicate minerals, along with the depletion of mobile elements, such as Na, Ca, and Mg [71,72]. Previous studies on silicate weathering have demonstrated that rivers tend to selectively accumulate lighter magnesium isotopes, while the residues enriched in the heavier Mg isotopes are transported by rivers into lakes [73–75]. Hence, when considering a certain period and a particular watershed comprehensively, the relationship between river-dissolved Mg during silicate weathering and weathering residues can be articulated as follows:

$$\delta^{26}\text{Mg}_{\text{sili}} = \delta^{26}\text{Mg}_{\text{resi}} + \Delta\delta^{26}\text{Mg}_{\text{fluid-protolith}} \quad (1)$$

where  $\delta^{26}\text{Mg}_{\text{sili}}$  and  $\delta^{26}\text{Mg}_{\text{resi}}$  represent the Mg isotope compositions of the dissolved Mg flux of silicate weathering and weathering residues, respectively.  $\Delta\delta^{26}\text{Mg}_{\text{fluid-protolith}}$  represents the Mg isotope fractionation factor between the dissolved Mg flux released by weathering and the silicate protolith.

The Mg budgets of rivers are mainly controlled by the chemical weathering of silicate minerals and the dissolution of carbonate [41]. Therefore, the Mg flux and isotope mass balance of the river input can be expressed by Equations (2) and (3) [76]:

$$F_{\text{riv}} = F_{\text{sili}} + F_{\text{car}} \quad (2)$$

$$F_{\text{riv}} \cdot \delta^{26}\text{Mg}_{\text{riv}} = F_{\text{sili}} \cdot \delta^{26}\text{Mg}_{\text{sili}} + F_{\text{car}} \cdot \delta^{26}\text{Mg}_{\text{car}} \quad (3)$$

where  $F_{\text{riv}}$  and  $F_{\text{sili}}$  represent the Mg flux of the river input and the dissolved Mg flux released by silicate weathering, respectively.  $F_{\text{car}}$  refers to the dissolved Mg flux released by carbonate weathering.  $\delta^{26}\text{Mg}_{\text{riv}}$  and  $\delta^{26}\text{Mg}_{\text{car}}$  represent the Mg isotope compositions of the dissolved Mg flux of river and carbonate weathering, respectively.

### 5.2.2. Numerical Model of Magnesium Cycling and Isotopic Mass Balance in Saline Lake

We performed major and trace element analyses on the water-washed solution of the samples C1 and C2 in the Qianjiang Formation, revealing that glauberite is the predominant evaporite mineral with a very low magnesium content (Table S2). This suggests that during the deposition period, the lake water had not yet reached the point of depositing Mg evaporite minerals. Consequently, the influence of water-soluble magnesium evaporite minerals on magnesium isotopes is very limited and thus negligible.

Authigenic clay minerals, formed at or near the sediment water interface, are usually rich in Mg, influencing the geochemical budget of lake waters and the properties of contemporaneous authigenic carbonate precipitates [77–79]. However, authigenic clay minerals usually form in saline and alkaline lake systems. In saline and alkaline lakes, authigenic minerals, such as Mg-rich clay minerals and Mg-rich evaporites, will compete for  $\text{Mg}^{2+}$  with dolomite [79,80]. In non-alkaline saline lakes, authigenic Mg minerals like Mg-rich clay and Mg-rich evaporites either precipitate to a minimal extent or do not deposit [21]. During the deposition of the Qianjiang Formation, the basin was characterized as a non-alkaline salt lake [21,81], leading to the minimal or negligible development of authigenic clay minerals, and the lack of Mg in evaporites can also support this (Table S2). Thus, we can rule out the influence of authigenic minerals including Mg clays and Mg evaporites. Hence, the Mg isotope compositions of the lake ( $\delta^{26}\text{Mg}_{\text{lake}}$ ) and the total lake water Mg

contents ( $N_{Mg}$ ) are only controlled by the annual Mg flux of rivers ( $F_{riv}$ ) into the lake and the annual outflux of dolomite precipitation ( $F_{dol}$ ). The dynamic changes in the amount of Mg and the Mg isotope mass balance of the lake can be described as follows [23,41,76]:

$$\frac{dN_{Mg}}{dt} = F_{riv} - F_{dol} \tag{4}$$

$$\frac{d\delta^{26}Mg_{lake}}{dt} = \left( \delta^{26}Mg_{riv} - \delta^{26}Mg_{lake} \right) \cdot \frac{F_{riv}}{N_{Mg}} - \Delta\delta^{26}Mg_{dol-lw} \cdot \frac{F_{dol}}{N_{Mg}} \tag{5}$$

where  $\Delta\delta^{26}Mg_{dol-lk}$  represents the Mg isotope fractionations associated with the formation of dolomite. At 25 °C,  $\Delta\delta^{26}Mg_{dol-lk}$  is 1.8‰ [82]. The model results are shown in Figure 6a. When  $F_{riv} > F_{dol}$ , the magnesium content ( $N_{Mg}$ ) continues to increase; the Mg isotope composition of the lake would decrease progressively if the influx of riverine  $\delta^{26}Mg$  was light. When  $F_{riv} < F_{dol}$ , the lake would be enriched in  $^{26}Mg$  during the dolomitization processes.  $N_{Mg}/F_{riv}$  and  $N_{Mg}/F_{dol}$  will affect the model’s result. We constrained this ratio using the centimeter-scale geochemical data of C1 and validated the model, as detailed in Section 5.2.5.

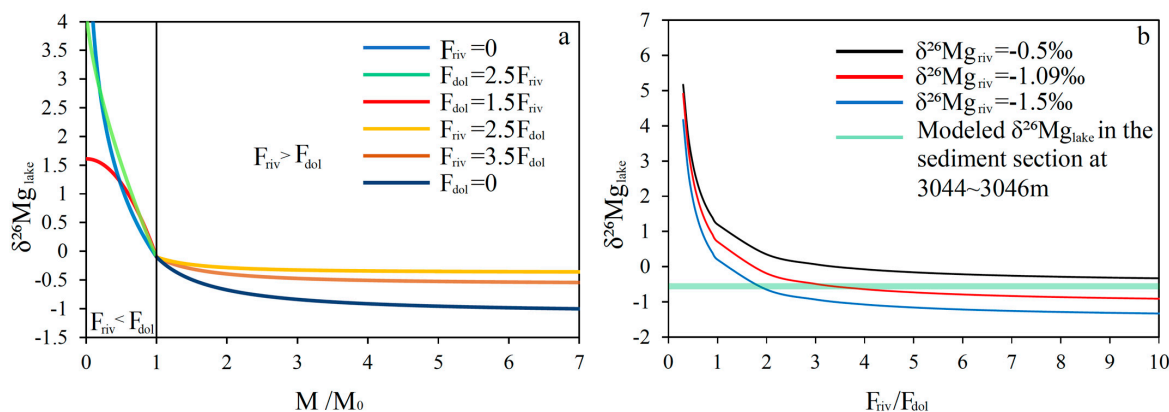


**Figure 6.** (a) Model results show the influence of dolomite precipitation and the riverine Mg input on the Mg isotope composition in the lake. ( $M_0$  represents the mass of Mg at the initial moment. The  $\delta^{26}Mg$  values of the initial lake water are set to  $-0.1\text{‰}$ . To simplify the model,  $F_{riv}$  and  $F_{dol}$  are set as constants.) (b) Schematic shows the likely response of  $\delta^{26}Mg$  in the lake by changing the proportion of the Mg sink between river input and dolomite precipitation when the  $\delta^{26}Mg$  of the lake remains stable. For details, see Supplementary text.

Otherwise, when  $\delta^{26}Mg_{lake}$  remains constant, it becomes a steady-state model, then Equation (5) can be simplified as follows:

$$\left( \delta^{26}Mg_{riv} - \delta^{26}Mg_{lake} \right) \cdot \frac{F_{riv}}{N_{Mg}} = \Delta\delta^{26}Mg_{dol-lw} \cdot \frac{F_{dol}}{N_{Mg}} \tag{6}$$

Hence,

$$\delta^{26}Mg_{lake} = \delta^{26}Mg_{riv} - \frac{\Delta\delta^{26}Mg_{dol-lw}}{\frac{F_{riv}}{F_{dol}}} \tag{7}$$

The model results of Equation (7) are shown in Figure 6b.

### 5.2.3. Dolomite Magnesium Isotope System Controlled by Riverine Input under Humid Climate Conditions

In the section at depths of 3044–3046 m,  $\delta^{26}Mg_{dol}$  remains relatively stable and predominantly negative, thereby essentially ruling out the occurrence of dolomitization processes in confined environments, as dolomitization would quickly increase the magnesium isotope values (Figure 6a). Therefore, we can use Equation (7) to simulate the changes in the Mg

isotopes of lake water (Figure 6b). The invariable  $\delta^{26}\text{Mg}_{\text{Si}}$  (ranging from 0.337 to 0.505‰, average = 0.405‰) values mean the dissolved Mg flux released by carbonate weathering in the source area is generally maintained in a stable state. Given that the Qianjiang Depression is a rift lake basin that formed in a volcanic background setting [44,64], we hypothesize a relatively minor contribution of carbonate weathering to Mg in riverine inputs. And thus, the Mg isotope composition of the river input remains stable in this section. River waters usually have low  $\delta^{26}\text{Mg}$  values (−2.52‰ to +0.64‰, averaging at −1.09‰) [8,41], so we employ −1.09‰ as the Mg isotope of the river input within this sediment section.

The model results indicate that the Mg flux from the river input is 3–4 times greater than that consumed by dolomite precipitation (Figure 6b). Thus, we set the  $F_{\text{riv}}/F_{\text{dol}}$  as 3.7 to simulate the Mg isotopes of the lake in this section. The model results suggest that with the increasing magnesium content in the lake, the magnesium isotopes in the lake water gradually become more negative and conform to our expected values (the modeled  $\delta^{26}\text{Mg}$  of lake water ranging from −0.60‰ to −0.52‰) when  $M/M_0$  exceeds 3 (Figure 6a). Furthermore, the relatively high CIA values and low  $\delta^{18}\text{O}_{\text{carb}}$  of the 3044~3046 m section both point to a strong weathering intensity and relatively humid climate, corresponding to the relatively high river input simulated by the model (Figure 7a).

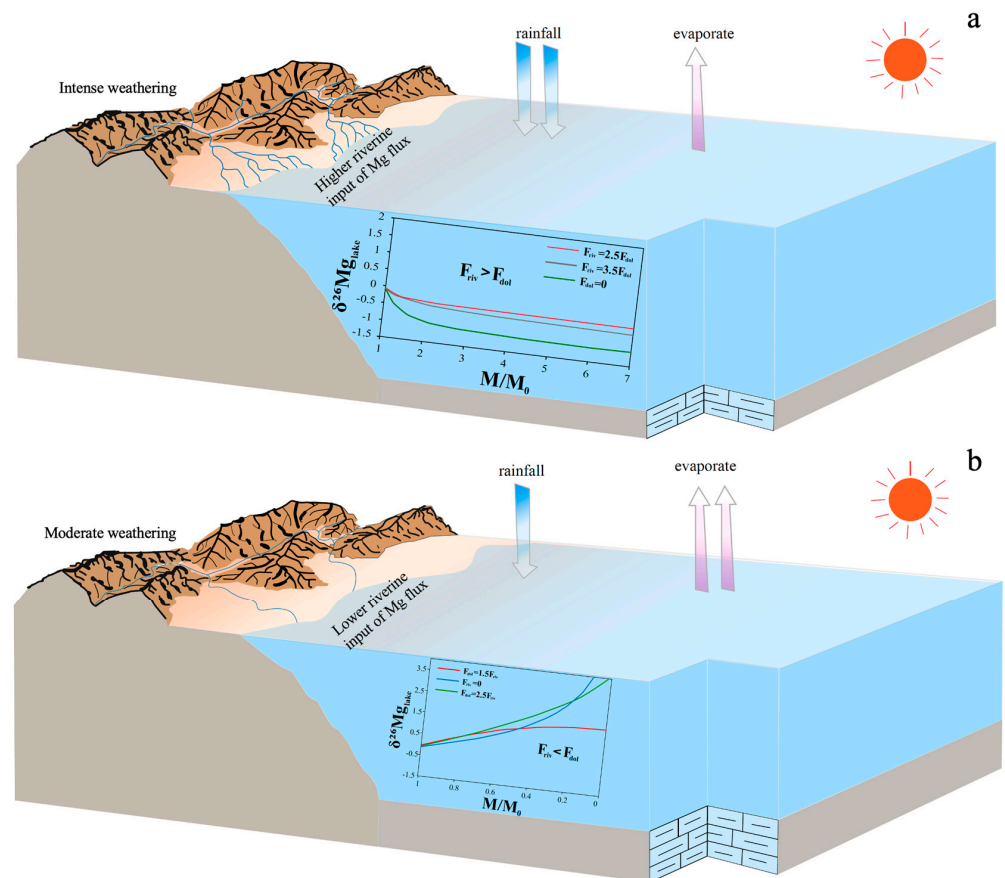


**Figure 7.** (a) During humid climates, the magnesium flux from river inputs exceeds the magnesium consumption by dolomite sedimentation, and river inputs dominate the magnesium isotopes of lake water. During this period, weathering intensity is high, while evaporation is weak, which is characterized by high CIA values, low  $\delta^{18}\text{O}$  values, and lower and relatively stable magnesium isotope values of dolomite; (b) during relatively dry climates, the magnesium flux from river inputs is less than the magnesium consumption by dolomite sedimentation, and dolomite sedimentation dominates the magnesium isotopes of lake water. During this period, weathering intensity is low, while evaporation is strong. This is characterized by low CIA values, high  $\delta^{18}\text{O}$  values, and higher magnesium isotope values of dolomite.

#### 5.2.4. Dolomite Magnesium Isotope System Controlled by Dolomite Precipitation under Relative Dry Climate Conditions

In the section between the depths of 3031–3044 m, the magnesium isotope values of dolomite are relatively high and exhibit a consistent increase, gradually shifting towards positive values. The Mg isotope values of the dolomite in this interval are relatively high, with some reaching up to 0.717‰, 0.825‰, and 0.857‰. Considering the fractionation effect during dolomitization ( $\Delta\delta^{26}\text{Mg}_{\text{dol-lk}} = 1.8\text{‰}$  at 25 °C), the magnesium isotope composition of the lake water during this period is estimated to exceed 1‰. The range of the magnesium isotope values in river water is approximately  $-2.52\text{‰}$  to  $0.64\text{‰}$  [8,41], and thus, it is implausible that the elevated magnesium isotope values in the lake water are due to significant input from river water. The relatively low CIA values and higher  $\delta^{18}\text{O}_{\text{carb}}$  (Figure 2) of the 3031~3044 m sediment section indicate a weaker weathering intensity and relatively relative dry climate, which suggests a relatively low river discharge. Thus, the magnesium isotope composition of the lake water in this sedimentary interval is mainly controlled by dolomite precipitation under relatively dry climatic conditions.

The ratio of the magnesium flux from the river input to the magnesium flux consumed by dolomite sedimentation will affect the rate of change in the magnesium isotope values of the lake water. However, due to the instability of the magnesium isotopes in both the dolomite and detrital components in this interval, it is difficult to deduce specific ratios through steady-state models. In the model depicting the mass balance of the Mg and Mg isotopes in the lake, when  $F_{\text{riv}} < F_{\text{dol}}$ , the lake tends to be enriched in  $^{26}\text{Mg}$  as dolomitization proceeds rapidly (Figure 6a). In addition, this section has relatively low CIA values and higher  $\delta^{18}\text{O}_{\text{carb}}$ , which suggests a relatively weak weathering intensity and relatively dry climate. Within this section, the lake is in an evaporative state, with the Mg output exceeding the input in the lake water. The dominant dolomite sedimentation will continuously be enriched in  $^{26}\text{Mg}$  in the lake water (Figure 7b).

#### 5.2.5. Magnesium Isotope Variations in Dolomite at the Centimeter Sedimentary Scale Provide Support for Macroscopic Sedimentary Scale Models

Detailed geochemical analyses were conducted at the centimeter scale on two core samples, C1 (7 cm) and C2 (9 cm), within the study area (Figure 2). The results of the major and trace element, carbon and oxygen isotope, and magnesium isotope measurements are displayed in Figure 8. During the C1 period, the proportion of carbonate gradually increases, and the Mg/Ca ratios also rise gradually, suggesting a progressive increase in  $F_{\text{dol}}$ . This leads to a gradual enrichment of  $^{26}\text{Mg}$  in dolomite. Subsequently, the  $\delta^{26}\text{Mg}$  values in dolomite remain relatively stable (approximately  $-0.74\text{‰}$ ). The  $\delta^{26}\text{Mg}$  values of the C1 dolomite indicate a gradual enrichment followed by an equilibrium process, predominantly influenced by the lake water in dolomite precipitation.

In our earlier discussions, in order to simplify the model, we set  $F_{\text{dol}}$  as a constant due to the frequent changes in the dolomite content and Mg/Ca ratios. In the first 1.8 cm of C1, however, we observed substantial changes: the carbonate content increased from 11.20% to 53.58%, while the Mg/Ca ratio increased from 0.35 to 0.58. These findings suggest that  $F_{\text{dol}}$  increased to approximately seven times that of its initial value. Concurrently, the  $\delta^{26}\text{Mg}$  value of the dolomite increases from  $-0.97\text{‰}$  to  $-0.72\text{‰}$ , with corresponding increases in the  $\delta^{26}\text{Mg}$  values of the lake water from  $0.83\text{‰}$  to  $1.08\text{‰}$ . The sedimentation rate of the Eq<sup>3</sup> member in the Qianjiang formation is 0.1 to 0.43 m/ka [47], so we take an average sedimentation rate of 22 cm/ka for the C1 period in this simulation. Within the first 1.8 cm of C1, the  $F_{\text{dol}}$  increases to seven times that of its original value (roughly calculated using the magnesium calcium ratio and carbonate content), resulting in an increase in the  $\delta^{26}\text{Mg}$  values of the lake water from  $0.83\text{‰}$  to  $1.08\text{‰}$ . The simulation results suggest durations of 80 years and 70 years when the  $\delta^{26}\text{Mg}$  values of the river range between  $-1.09\text{‰}$  and  $-0.5\text{‰}$ , respectively (Figure 9). These simulated durations align with the calculated result obtained using the sedimentation rate (81.81 years).

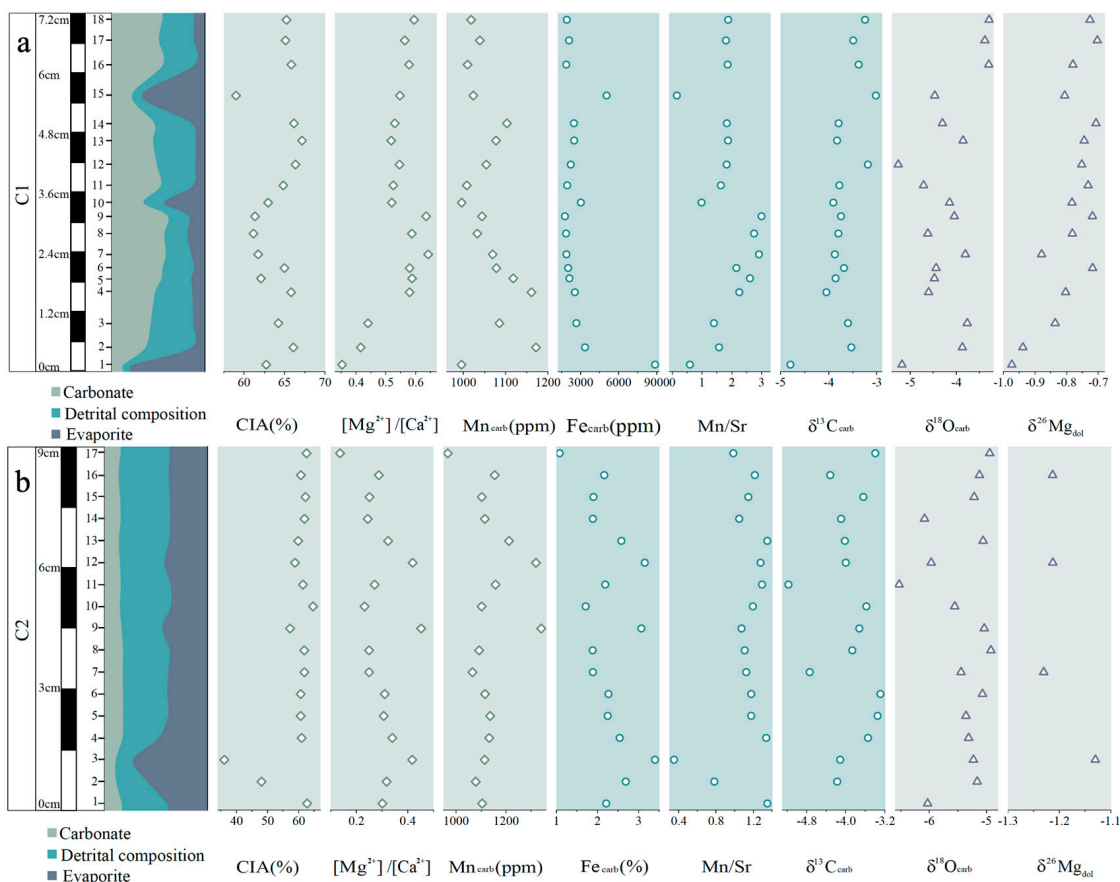


**Figure 8.** (a) Chemostratigraphic profiles of CIA,  $[Mg^{2+}]/[Ca^{2+}]$ , [Mn], [Fe], [Mn]/[Sr],  $\delta^{13}C_{carb}$ ,  $\delta^{18}O_{carb}$ , and  $\delta^{26}Mg_{dol}$  values of C1; (b) chemostratigraphic profiles of CIA,  $[Mg]/[Ca]$ , [Mn], [Fe], [Mn]/[Sr],  $\delta^{13}C_{carb}$ ,  $\delta^{18}O_{carb}$ , and  $\delta^{26}Mg_{dol}$  values of C2.

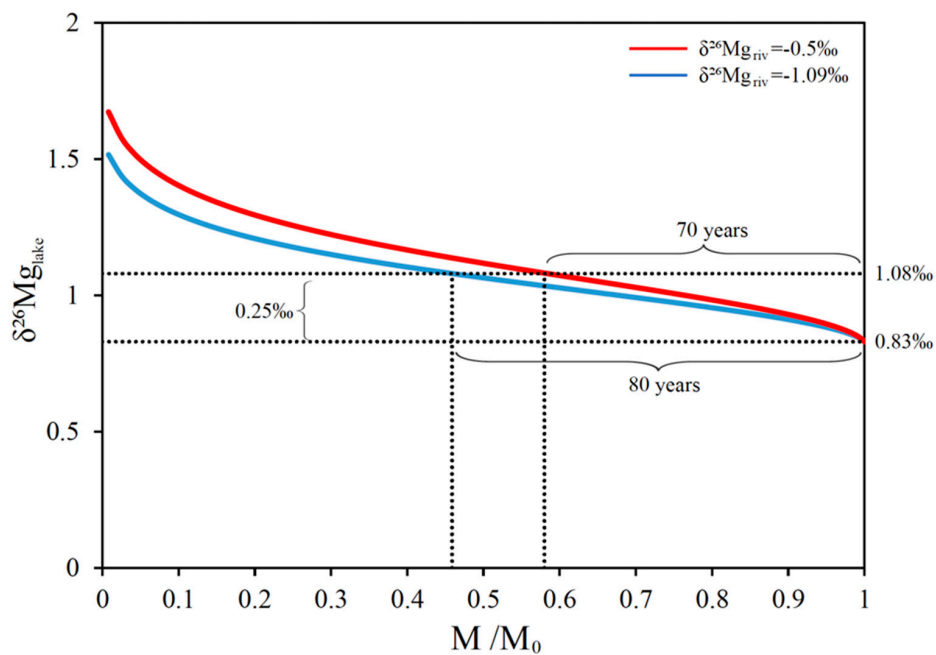


**Figure 9.** Results show that under river inputs with magnesium isotope values of  $-1.09\text{‰}$  and  $-0.5\text{‰}$ , after 80 years and 70 years, respectively, with  $F_{dol}$  growing 6.925 and 6.175 times as much as before, the Mg isotopes of lake water increased by  $0.25\text{‰}$ . For more details, see Supplementary text.

## 6. Conclusions

In this study, we identified two different dolomitization patterns under humid and relatively dry climatic conditions. Subsequently, we established a model to assess the lake magnesium flux and magnesium isotope mass balance, simulating the magnesium isotopes of the lake water under both scenarios. Under humid climatic conditions, the heightened Mg flux of the river inputs weakens the fractionation of the Mg isotopes during dolomite formation. This leads to an overall negative shift and the relative stability of the Mg isotopes in the lake water. Under relatively dry climatic conditions, the lower Mg flux of the river inputs results in dolomite magnesium isotope fractionation dominating the variation in the Mg isotopes in the lake water during dolomite formation. With the continuous precipitation of dolomite, the magnesium isotope in the lake water gradually becomes heavier, and the magnesium isotope of the subsequent dolomite formation also becomes heavier. The simulation of dolomite magnesium isotopes at the centimeter sedimentary scale confirms the reliability of our model.

**Supplementary Materials:** The following supporting information can be downloaded at <https://www.mdpi.com/article/10.3390/min14050459/s1>, Table S1: Element compositions of water washing components of C1 and L1-5 in Well BX-7 from the Qianjiang Depression, Jiangnan Basin; Table S2: Element compositions and isotopes of samples in Well BX-7 from the Qianjiang Depression, Jiangnan Basin; Supplementary text: Model data for Figures 6 and 9.

**Author Contributions:** Conceptualization, T.W.; methodology, T.W.; validation, K.L. and R.W.; formal analysis, T.W. and K.L.; investigation, T.W.; resources, R.W. and K.L.; data curation, T.W. and K.L.; writing—original draft preparation, T.W.; writing—review and editing, L.D.; supervision, L.D.; project administration, L.D.; funding acquisition, L.D. All authors have read and agreed to the published version of the manuscript.

**Funding:** This research was funded by the National Natural Science Foundation of China, grant number 42090021 and 42373050.

**Data Availability Statement:** Data will be made available on request.

**Conflicts of Interest:** The authors declare no conflicts of interest.

## References

1. Land, L.S. Failure to Precipitate Dolomite at 25 °C from Dilute Solution Despite 1000-Fold Oversaturation after 32 Years. *Aquat. Geochem.* **1998**, *4*, 361–368. [[CrossRef](#)]
2. Sibley, D. Dolomites: A Volume in Honour of Dolomieu. Bruce Purser, Maurice Tucker, Donald Zenger. *J. Geol.* **1995**, *103*, 729. [[CrossRef](#)]
3. Machel, H.G. Concepts and models of dolomitization; a critical reappraisal. *Geol. Soc. Spec. Publ.* **2004**, *235*, 7–63. [[CrossRef](#)]
4. Braithwaite, C.J.R.; Rizzi, G.; Darke, G. The Geometry and Petrogenesis of Dolomite Hydrocarbon Reservoirs. *Geol. Soc. Lond.* **2004**, *235*, 1–6. [[CrossRef](#)]
5. Liu, Q.; Zhu, D.; Jin, Z.; Liu, C.; Zhang, D.; He, Z. Coupled alteration of hydrothermal fluids and thermal sulfate reduction (TSR) in ancient dolomite reservoirs—An example from Sinian Dengying Formation in Sichuan Basin, Southern China. *Precambrian Res.* **2016**, *285*, 39–57. [[CrossRef](#)]
6. Johnson, C.; Beard, B.L.; Albarède, F. *Geochemistry of Non-Traditional Stable Isotopes*; Reviews in Mineralogy & Geochemistry Series; De Gruyter: Berlin, Germany, 2004; Volume 55. [[CrossRef](#)]
7. Geske, A.; Goldstein, R.H.; Mavromatis, V.; Richter, D.K.; Buhl, D.; Kluge, T.; John, C.M.; Immenhauser, A. The magnesium isotope ( $\delta^{26}\text{Mg}$ ) signature of dolomites. *Geochim. Cosmochim. Acta* **2015**, *149*, 131–151. [[CrossRef](#)]
8. Teng, F.-Z. Magnesium isotope Geochemistry. *Rev. Mineral. Geochem.* **2017**, *82*, 219–287. [[CrossRef](#)]
9. Li, J.; Hao, C.; Wang, Z.; Dong, L.; Wang, Y.; Huang, K.-J.; Lang, X.; Huang, T.; Yuan, H.; Zhou, C.; et al. Continental weathering intensity during the termination of the Marinoan Snowball Earth: Mg isotope evidence from the basal Doushantuo cap carbonate in South China. *Palaeogeogr. Palaeoclimatol. Palaeoecol.* **2020**, *552*, 109774. [[CrossRef](#)]
10. Teng, F.-Z.; Li, W.-Y.; Rudnick, R.L.; Gardner, L.R. Contrasting lithium and magnesium isotope fractionation during continental weathering. *Earth Planet. Sci. Lett.* **2010**, *300*, 63–71. [[CrossRef](#)]
11. Galy, A.; Bar-Matthews, M.; Halicz, L.; O’Nions, R.K. Mg isotopic composition of carbonate: Insight from speleothem formation. *Earth Planet. Sci. Lett.* **2002**, *201*, 105–115. [[CrossRef](#)]
12. Wimpenny, J.; Burton, K.W.; James, R.H.; Gannoun, A.; Mokadem, F.; Gislason, S.R. The behaviour of magnesium and its isotopes during glacial weathering in an ancient shield terrain in West Greenland. *Earth Planet. Sci. Lett.* **2011**, *304*, 260–269. [[CrossRef](#)]

13. Fantle, M.S.; Higgins, J. The effects of diagenesis and dolomitization on Ca and Mg isotopes in marine platform carbonates: Implications for the geochemical cycles of Ca and Mg. *Geochim. Cosmochim. Acta* **2014**, *142*, 458–481. [[CrossRef](#)]
14. Wimpenny, J.; Colla, C.A.; Yin, Q.Z.; Rustad, J.R.; Casey, W.H. Investigating the behaviour of Mg isotopes during the formation of clay minerals. *Geochim. Cosmochim. Acta* **2014**, *128*, 178–194. [[CrossRef](#)]
15. Huang, K.-J.; Shen, B.; Xianguo, L.; Tang, W.-B.; Yang, P.; Shan, K.; Kaufman, A.J.; Haoran, M.; Fangbing, L. Magnesium isotopic compositions of the Mesoproterozoic dolostones: Implications for Mg isotopic systematics of marine carbonates. *Geochim. Cosmochim. Acta* **2015**, *164*, 333–351. [[CrossRef](#)]
16. Peng, Y.; Shen, B.; Lang, X.-G.; Huang, K.-J.; Chen, J.-T.; Yan, Z.; Tang, W.-B.; Ke, S.; Ma, H.-R.; Li, F.-B. Constraining dolomitization by Mg isotopes: A case study from partially dolomitized limestones of the middle Cambrian Xuzhuang Formation, North China. *Geochim. Geophys. Geosystems* **2016**, *17*, 1109–1129. [[CrossRef](#)]
17. Ning, M.; Lang, X.; Huang, K.; Li, C.; Huang, T.; Yuan, H.; Xing, C.; Yang, R.; Shen, B. Towards understanding the origin of massive dolostones. *Earth Planet. Sci. Lett.* **2020**, *545*, 116403. [[CrossRef](#)]
18. Labuhn, I.; Tell, F.; von Grafenstein, U.; Hammarlund, D.; Kuhnert, H.; Minster, B. A modern snapshot of the isotopic composition of lacustrine biogenic carbonates—Records of seasonal water temperature variability. *Biogeosciences* **2022**, *19*, 2759–2777. [[CrossRef](#)]
19. Martin, J.B. Carbonate minerals in the global carbon cycle. *Chem. Geol.* **2017**, *449*, 58–72. [[CrossRef](#)]
20. Wang, Y.; Wu, C.; Fang, Y.; Ma, J.; Shen, B.; Huang, F.; Li, L.; Ning, M.; Zhai, L.; Zhang, W. Mg, C and O isotopic compositions of Late Cretaceous lacustrine dolomite and travertine in the northern Tianshan Mountains, Northwest China. *Chem. Geol.* **2020**, *541*, 119569. [[CrossRef](#)]
21. Guo, P.; Wen, H.; Li, C.; He, H.; Sánchez-Román, M. Lacustrine dolomite in deep time: What really matters in early dolomite formation and accumulation? *Earth-Sci. Rev.* **2023**, *246*, 104575. [[CrossRef](#)]
22. Wei, R.; Ma, H.; Jin, Z.; Wang, T.; Zhang, C.; Wang, Y.; Dong, L. New insights into the carbon cycle and depositional models of the Eocene saline lake, Jiangnan basin, China. *Mar. Pet. Geol.* **2023**, *149*, 106079. [[CrossRef](#)]
23. Xia, Z.; Lin, Y.; Wei, H.; Hu, Z.; Liu, C.; Li, W. Reconstruct hydrological history of terrestrial saline lakes using Mg isotopes in halite: A case study of the Quaternary Dalangtan playa in Qaidam Basin, NW China. *Palaeogeogr. Palaeoclimatol. Palaeoecol.* **2022**, *587*, 110804. [[CrossRef](#)]
24. Ning, M.; Wang, Y.; McKenzie, J.A.; Vasconcelos, C.; Li, C.; Shen, A.; Liang, F.; Shen, B. Dolomite formation during penecontemporaneous subaerial diagenesis: Evidence from modern dolomite crusts forming in lagoon Brejo do Espinho, Brazil. *J. Geol. Soc.* **2024**, *181*, 159. [[CrossRef](#)]
25. Shalev, N.; Bontognali, T.R.R.; Vance, D. Sabkha dolomite as an archive for the magnesium isotope composition of seawater. *Geology* **2020**, *49*, 253–257. [[CrossRef](#)]
26. Arribas, M.E.; Bustillo, A.; Tsige, M. Lacustrine chalky carbonates: Origin, physical properties and diagenesis (Palaeogene of the Madrid Basin, Spain). *Sediment. Geol.* **2004**, *166*, 335–351. [[CrossRef](#)]
27. Boak, J.; Poole, S. Mineralogy of the Green River Formation in the Piceance Creek Basin, Colorado. In *Stratigraphy and Paleolimnology of the Green River Formation, Western USA*; Springer: Dordrecht, The Netherlands, 2015; Volume 1, pp. 183–209.
28. Bustillo, M.A.; Arribas, M.E.; Bustillo, M. Dolomitization and silicification in low-energy lacustrine carbonates (Paleogene, Madrid Basin, Spain). *Sediment. Geol.* **2002**, *151*, 107–126. [[CrossRef](#)]
29. Calvo, J.P.; Jones, B.F.; Bustillo, M.; Fort, R.; Alonso Zarza, A.M.; Kendall, C. Sedimentology and geochemistry of carbonates from lacustrine sequences in the Madrid Basin, central Spain. *Chem. Geol.* **1995**, *123*, 173–191. [[CrossRef](#)]
30. Casado, A.I.; Alonso-Zarza, A.M.; La Iglesia, Á. Morphology and origin of dolomite in paleosols and lacustrine sequences. Examples from the Miocene of the Madrid Basin. *Sediment. Geol.* **2014**, *312*, 50–62. [[CrossRef](#)]
31. Donnelly, T.H.; Jackson, M.J. Sedimentology and geochemistry of a mid-Proterozoic lacustrine unit from northern Australia. *Sediment. Geol.* **1988**, *58*, 145–169. [[CrossRef](#)]
32. García Del Cura, M.A.; Calvo, J.P.; Ordóñez, S.; Jones, B.F.; Cañaveras, J.C. Petrographic and geochemical evidence for the formation of primary, bacterially induced lacustrine dolomite: La Roda ‘white earth’ (Pliocene, central Spain). *Sedimentology* **2001**, *48*, 897–915. [[CrossRef](#)]
33. Janaway, T.M.; Parnell, J. Carbonate production within the orcadian basin, Northern Scotland: A petrographic and geochemical study. *Palaeogeogr. Palaeoclimatol. Palaeoecol.* **1989**, *70*, 89–105. [[CrossRef](#)]
34. Murphy, J.T.; Lowenstein, T.K.; Pietras, J.T. Preservation of primary lake signatures in alkaline earth carbonates of the Eocene Green River Wilkins Peak-Laney Member transition zone. *Sediment. Geol.* **2014**, *314*, 75–91. [[CrossRef](#)]
35. Sánchez-Román, M.; McKenzie, J.A.; de Luca Rebello Wagener, A.; Rivadeneyra, M.A.; Vasconcelos, C. Presence of sulfate does not inhibit low-temperature dolomite precipitation. *Earth Planet. Sci. Lett.* **2009**, *285*, 131–139. [[CrossRef](#)]
36. Sánchez-Román, M.; Vasconcelos, C.; Schmid, T.; Dittrich, M.; McKenzie, J.A.; Zenobi, R.; Rivadeneyra, M.A. Aerobic microbial dolomite at the nanometer scale: Implications for the geologic record. *Geology* **2008**, *36*, 879–882. [[CrossRef](#)]
37. Shaked Gelband, D.; Edelman-Furstenberg, Y.; Stein, M.; Starinsky, A. Formation of lacustrine dolomite in the late Miocene marginal lakes of the East Mediterranean (Northern Israel). *Sedimentology* **2019**, *66*, 2950–2975. [[CrossRef](#)]
38. Valero Garcés, B.L. Lacustrine deposition and related volcanism in a transtensional tectonic setting: Upper Stephanian-Lower Autunian in the Aragón-Béarn Basin, western Pyrenees (Spain-France). *Sediment. Geol.* **1993**, *83*, 133–160. [[CrossRef](#)]
39. Wanas, H.A.; Sallam, E. Abiotically-formed, primary dolomite in the mid-Eocene lacustrine succession at Gebel El-Goza El-Hamra, NE Egypt: An approach to the role of smectitic clays. *Sediment. Geol.* **2016**, *343*, 132–140. [[CrossRef](#)]

40. Zhang, H.; Jiang, X.-W.; Wan, L.; Ke, S.; Liu, S.-A.; Han, G.; Guo, H.; Dong, A. Fractionation of Mg isotopes by clay formation and calcite precipitation in groundwater with long residence times in a sandstone aquifer, Ordos Basin, China. *Geochim. Cosmochim. Acta* **2018**, *237*, 261–274. [[CrossRef](#)]
41. Tipper, E.T.; Galy, A.; Gaillardet, J.; Bickle, M.J.; Elderfield, H.; Carder, E.A. The magnesium isotope budget of the modern ocean: Constraints from riverine magnesium isotope ratios. *Earth Planet. Sci. Lett.* **2006**, *250*, 241–253. [[CrossRef](#)]
42. Herlinger, R., Jr.; Zambonato, E.E.; De Ros, L.F. Influence of Diagenesis On the Quality of Lower Cretaceous Pre-salt Lacustrine Carbonate Reservoirs from Northern Campos Basin, Offshore Brazil. *J. Sediment. Res.* **2017**, *87*, 1285–1313. [[CrossRef](#)]
43. Zhang, J.; Liu, G.; Cao, Z.; Tao, S.; Felix, M.; Kong, Y.; Zhang, Y. Characteristics and formation mechanism of multi-source mixed sedimentary rocks in a saline lake, a case study of the Permian Lucaogou Formation in the Jimusaer Sag, northwest China. *Mar. Pet. Geol.* **2019**, *102*, 704–724. [[CrossRef](#)]
44. Wu, L.; Mei, L.; Paton, D.A.; Guo, P.; Liu, Y.; Luo, J.; Wang, D.; Li, M.; Zhang, P.; Wen, H. Deciphering the origin of the Cenozoic intracontinental rifting and volcanism in eastern China using integrated evidence from the Jiangnan Basin. *Gondwana Res.* **2018**, *64*, 67–83. [[CrossRef](#)]
45. Kong, X.; Jiang, Z.; Ju, B.; Liang, C.; Cai, Y.; Wu, S. Fine-grained carbonate formation and organic matter enrichment in an Eocene saline rift lake (Qianjiang Depression): Constraints from depositional environment and material source. *Mar. Pet. Geol.* **2022**, *138*, 105534. [[CrossRef](#)]
46. Li, M.; Chen, Z.; Qian, M.; Ma, X.; Jiang, Q.; Li, Z.; Tao, G.; Wu, S. What are in pyrolysis S1 peak and what are missed? Petroleum compositional characteristics revealed from programmed pyrolysis and implications for shale oil mobility and resource potential. *Int. J. Coal Geol.* **2020**, *217*, 103321. [[CrossRef](#)]
47. Huang, C.; Hinnov, L. Evolution of an Eocene–Oligocene saline lake depositional system and its controlling factors, Jiangnan Basin, China. *J. Earth Sci.* **2014**, *25*, 959–976. [[CrossRef](#)]
48. Fang, Q.; Li, Y. Exhaustive brine production and complete CO<sub>2</sub> storage in Jiangnan Basin of China. *Environ. Earth Sci.* **2014**, *72*, 1541–1553. [[CrossRef](#)]
49. Xu, L.; Yan, C.; Yu, H.; Wang, B.; Yu, F.; Wang, D. Chronology of Paleogene volcanic rocks in Jiangnan Basin. *Oil Gas Geol.* **1995**, *16*, 132–137.
50. Nie, X.; Lu, J.; Djaroun, R.R.; Wang, P.; Li, J.; Zhang, C. Oil content prediction of lacustrine organic-rich shale from wireline logs: A case study of intersalt reservoirs in the Qianjiang Sag, Jiangnan Basin, China. *Interpretation* **2020**, *8*, SL79–SL88. [[CrossRef](#)]
51. Accordi, G.; Carbone, F. Evolution of the siliciclastic-carbonate shelf system of the northern Kenyan coastal belt in response to Late Pleistocene–Holocene relative sea level changes. *J. Afr. Earth Sci.* **2016**, *123*, 234–257. [[CrossRef](#)]
52. Shen, J.J.; Chen, K.Q.; Liu, Y.; Chen, F.F.; Qiu, X.S.; Ma, X.Q.; Meng, J.H. Sedimentary facies of Paleogene lacustrine dolomicrite and implications for petroleum reservoirs in the southern Qianjiang Depression, China. *Open Geosci.* **2019**, *11*, 513–532. [[CrossRef](#)]
53. Galy, A.; Yoffe, O.; Janney, P.E.; Williams, R.W.; Cloquet, C.; Alard, O.; Halicz, L.; Wadhwa, M.; Hutcheon, I.D.; Ramon, E.; et al. Magnesium isotope heterogeneity of the isotopic standard SRM980 and new reference materials for magnesium-isotope-ratio measurements. *J. Anal. At. Spectrom.* **2003**, *18*, 1352–1356. [[CrossRef](#)]
54. Bao, Z.; Huang, K.; Huang, T.; Shen, B.; Zong, C.; Chen, K.; Yuan, H. Precise magnesium isotope analyses of high-K and low-Mg rocks by MC-ICP-MS. *J. Anal. At. Spectrom.* **2019**, *34*, 940–953. [[CrossRef](#)]
55. Jacobsen, S.B.; Kaufman, A.J. The Sr, C and O isotopic evolution of Neoproterozoic seawater. *Chem. Geol.* **1999**, *161*, 37–57. [[CrossRef](#)]
56. Knauth, L.P.; Kennedy, M.J. The late Precambrian greening of the Earth. *Nature* **2009**, *460*, 728–732. [[CrossRef](#)] [[PubMed](#)]
57. Gómez Peral, L.E.; Poiré, D.G.; Strauss, H.; Zimmermann, U. Chemostratigraphy and diagenetic constraints on Neoproterozoic carbonate successions from the Sierras Bayas Group, Tandilia System, Argentina. *Chem. Geol.* **2007**, *237*, 109–128. [[CrossRef](#)]
58. Brand, U.; Veizer, J. Chemical Diagenesis of a Multicomponent Carbonate System; 1, Trace-Elements. *J. Sediment. Res.* **1980**, *50*, 1219–1236. [[CrossRef](#)]
59. Moradi, A.V.; Sari, A.; Akkaya, P. Geochemistry of the Miocene oil shale (Hancili Formation) in the Cankiri-Corum Basin, Central Turkey: Implications for Paleoclimate conditions, source-area weathering, provenance and tectonic setting. *Sediment. Geol.* **2016**, *341*, 289–303. [[CrossRef](#)]
60. Critelli, S.; Mongelli, G.; Perri, F.; Martín-Algarra, A.; Martín-Martín, M.; Perrone, V.; Dominici, R.; Sonnino, M.; Zaghoul, M.N. Compositional and Geochemical Signatures for the Sedimentary Evolution of the Middle Triassic–Lower Jurassic Continental Redbeds from Western-Central Mediterranean Alpine Chains. *J. Geol.* **2008**, *116*, 375–386. [[CrossRef](#)]
61. Nesbitt, H.W.; Young, G.M. Early Proterozoic climates and plate motions inferred from major element chemistry of lutites. *Nature* **1982**, *299*, 715–717. [[CrossRef](#)]
62. Fedo, C.M.; Nesbitt, H.W.; Young, G.M. Unraveling the effects of potassium metasomatism in sedimentary rocks and paleosols, with implications for paleoweathering conditions and provenance. *Geology* **1995**, *23*, 921–924. [[CrossRef](#)]
63. Hillman, A.L.; O’Quinn, R.F.; Abbott, M.B.; Bain, D.J. A Holocene history of the Indian monsoon from Qilu Lake, southwestern China. *Quat. Sci. Rev.* **2020**, *227*, 106051. [[CrossRef](#)]
64. Dai, S. *Petroleum Geology of Jiangnan Saline Basin*; Petroleum Industry Publishing House: Beijing, China, 1997.
65. Taylor, S.G.; Bradley, C.E. Optimal Ordering Strategies for Announced Price Increases. *Oper. Res.* **1985**, *33*, 237–468. [[CrossRef](#)]
66. Bhatia, M.R.; Crook, K.A.W. Trace element characteristics of graywackes and tectonic setting discrimination of sedimentary basins. *Contrib. Mineral. Petrol.* **1986**, *92*, 181–193. [[CrossRef](#)]

67. Cullers, R.L.; Podkovyrov, V.N. Geochemistry of the Mesoproterozoic Lakhanda shales in southeastern Yakutia, Russia: Implications for mineralogical and provenance control, and recycling. *Precambrian Res.* **2000**, *104*, 77–93. [[CrossRef](#)]
68. Floyd, P.A.; Leveridge, B.E. Tectonic environment of the Devonian Gramscatho basin, south Cornwall: Framework mode and geochemical evidence from turbiditic sandstones. *J. Geol. Soc.* **1987**, *144*, 531–542. [[CrossRef](#)]
69. Cullers, R.L. Implications of elemental concentrations for provenance, redox conditions, and metamorphic studies of shales and limestones near Pueblo, CO, USA. *Chem. Geol.* **2002**, *191*, 305–327. [[CrossRef](#)]
70. Li, W.; Bialik, O.M.; Wang, X.; Yang, T.; Hu, Z.; Huang, Q.; Zhao, S.; Waldmann, N.D. Effects of early diagenesis on Mg isotopes in dolomite: The roles of Mn(IV)-reduction and recrystallization. *Geochim. Cosmochim. Acta* **2019**, *250*, 1–17. [[CrossRef](#)]
71. Gaillardet, J.; Dupré, B.; Louvat, P.; Allègre, C.J. Global silicate weathering and CO<sub>2</sub> consumption rates deduced from the chemistry of large rivers. *Chem. Geol.* **1999**, *159*, 3–30. [[CrossRef](#)]
72. Penman, D.E.; Caves Rügenstein, J.K.; Ibarra, D.E.; Winnick, M.J. Silicate weathering as a feedback and forcing in Earth’s climate and carbon cycle. *Earth-Sci. Rev.* **2020**, *209*, 103298. [[CrossRef](#)]
73. Liu, X.-M.; Teng, F.-Z.; Rudnick, R.L.; McDonough, W.F.; Cummings, M.L. Massive magnesium depletion and isotope fractionation in weathered basalts. *Geochim. Cosmochim. Acta* **2014**, *135*, 336–349. [[CrossRef](#)]
74. Guo, B.; Zhu, X.; Dong, A.; Yan, B.; Shi, G.; Zhao, Z. Mg isotopic systematics and geochemical applications: A critical review. *J. Asian Earth Sci.* **2019**, *176*, 368–385. [[CrossRef](#)]
75. Tipper, E.T.; Galy, A.; Bickle, M.J. Riverine evidence for a fractionated reservoir of Ca and Mg on the continents: Implications for the oceanic Ca cycle. *Earth Planet. Sci. Lett.* **2006**, *247*, 267–279. [[CrossRef](#)]
76. Hu, Z.; Yang, S.; Yang, C.; Guo, Y.; Xu, J.; Zhang, C. Mg isotopes of siliciclastic sediments on continental marginal sea: Insights for the potential to trace silicate weathering. *Glob. Planet. Change* **2023**, *231*, 104307. [[CrossRef](#)]
77. Bristow, T.F.; Kennedy, M.J.; Morrison, K.D.; Mrofka, D.D. The influence of authigenic clay formation on the mineralogy and stable isotopic record of lacustrine carbonates. *Geochim. Cosmochim. Acta* **2012**, *90*, 64–82. [[CrossRef](#)]
78. Deocampo, D.M. Chapter 1 The Geochemistry of Continental Carbonates. *Dev. Sedimentol.* **2010**, *62*, 1–59. [[CrossRef](#)]
79. Jones, B.F.; Deocampo, D.M. Geochemistry of Saline Lakes. *Treatise Geochem.* **2013**, *437*, 393–424.
80. Shalev, N.; Lazar, B.; Halicz, L.; Gavrieli, I. The Mg isotope signature of marine Mg-evaporites. *Geochim. Cosmochim. Acta* **2021**, *301*, 30–47. [[CrossRef](#)]
81. Zhang, Y.; Hou, X.; Zhang, H. Sedimentary characteristics and formation mechanism of penepimentary dolostone in the Upper Eocene salt-bearing interval in Qianjiang Sag, Jiangnan Basin. *J. Palaeogeogr.* **2006**, *8*, 441–455.
82. Li, W.; Beard, B.L.; Li, C.; Xu, H.; Johnson, C.M. Experimental calibration of Mg isotope fractionation between dolomite and aqueous solution and its geological implications. *Geochim. Cosmochim. Acta* **2015**, *157*, 164–181. [[CrossRef](#)]

**Disclaimer/Publisher’s Note:** The statements, opinions and data contained in all publications are solely those of the individual author(s) and contributor(s) and not of MDPI and/or the editor(s). MDPI and/or the editor(s) disclaim responsibility for any injury to people or property resulting from any ideas, methods, instructions or products referred to in the content.